ACS APPLIED ELECTRONIC MATERIALS

pubs.acs.org/acsaelm Article

Short-Term Facilitation-Then-Depression Enables Adaptive Processing of Sensory Inputs by Ion Channels in Biomolecular Synapses

Joshua J. Maraj,[#] Joseph S. Najem,[*,#] Jessie D. Ringley, Ryan J. Weiss, Garrett S. Rose, and Stephen A. Sarles[*]

Cite This: *ACS Appl. Electron. Mater.* 2021, 3, 4448−4458 Read Online

ACCESS | Metrics & More | Article Recommendations | Supporting Information

ABSTRACT: Providing AI platforms with perceptual capabilities at low energy cost is imperative to making them more human-like. This goal is contingent on developing stimuli-responsive materials that closely emulate diverse synaptic functions needed to enhance machine learning applications. Here a biomolecular device is reported, consisting of an insulating lipid membrane doped with voltage-activated, ion channel-forming monazomycin (Mz) species, that display diode-like current−voltage characteristics and emulate short-term *facilitation*-then-*depression* on time scales relevant to habituation in human sensory systems. Subjected to a slow train of voltage pulses, devices show only facilitation upon Mz channel formation. At higher pulse rates, faster facilitation creates later depression upon Mz inactivation. The device is integrated as a biomolecular synapse in an organic−inorganic hybrid afferent model to demonstrate its ability to process sensory inputs and mimic bidirectional retinal adaptation and sensitization. These findings highlight the value of instilling complex synaptic plasticity into engineered systems, which is useful for adaptive neuroprosthetics and biosignal processing.

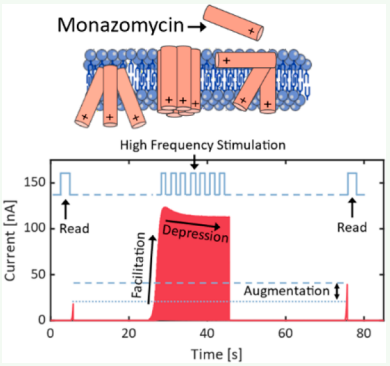

KEYWORDS: *monazomycin, artificial synapse, neuromorphic, short-term plasticity, biomolecular, habituation, volatile memristor, sensory processing*

1. INTRODUCTION

Despite rapid adoption, AI still lacks the necessary perceptual and cognitive abilities to perform human-like autonomous operation, learning, and decision-making.[1] Next-generation technologies based on materials with brain-like intelligence will not only enable AI to better perceive and understand the world around them, leading to more streamlined integration, but it will also drastically reduce power consumption.[2,3] Modern approaches to achieve this goal often leverage computing chips that model the brain's architecture for efficient signal processing.[4] Besides computing, brain-like sensory systems capable of extracting meaningful information from sparse data[5] and synapse-inspired materials such as memristors, whose values of electrical (or ionic) resistance depend on both past and present applied biases, offer memory and learning abilities at low power and footprint costs. In particular, materials that exhibit transient, activity-dependent changes in their electrical properties are deemed critical for supporting adaptive sensory processing and perceptual learning tasks in robots.[6,7]

While many current memristors successfully emulate features of long-term synaptic plasticity[8−10] and stable memory retention, few devices integrate one or more of the diverse forms of short-term plasticity (STP), such as short-term facilitation or depression.[10−15] STP refers to short-lived (milliseconds to minutes), activity-dependent changes of synaptic strength, a principle response for enabling sensory computing and perceptual learning.[16] Importantly, variations in synaptic strength during STP are not always unidirectional or monotonic. For instance, synaptic connections can get stronger at some firing frequencies, but weaker at others—a form of adaptive filtering.[16,17] Other forms of complex STP include adaptation and sensitization, dynamic gain control, and sensory timing, where both amplitude and duration of stimulation matter.[16] With the many types of plasticity possible in biological neural networks and their lower metabolic cost,[18] STP is central to both the sheer flexibility and high energy efficiency of the brain.

STP occurs in a presynaptic terminal when two or more action potentials arrive in close succession.[19,20] Two scenarios of response can arise: facilitation (i.e., an increase in synapse conductance) resulting from prolonged elevation of presynap-

Received: July 9, 2021
Published: September 16, 2021

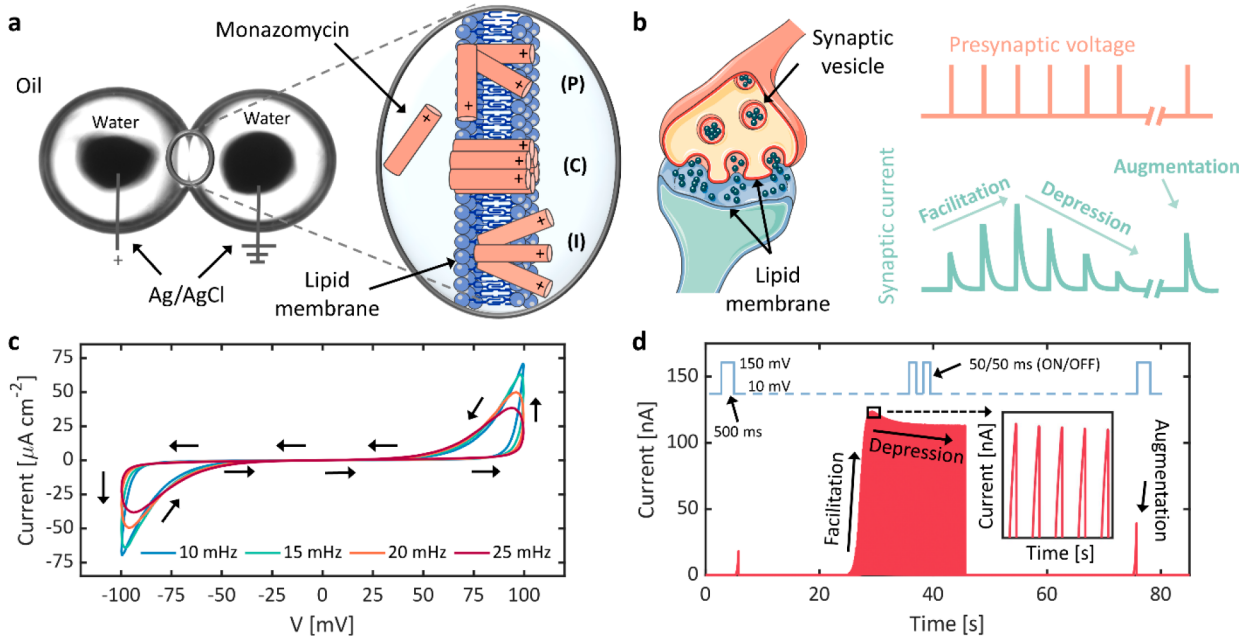

Figure 1. Mz-doped biomolecular synapses (MzBS) mimic STP in biological synapses. (a) A two-terminal, biomolecular synapse consisting of a Mz-doped lipid membrane formed between two droplets of water in oil immobilized by inserted Ag/AgCl electrodes as seen from below. The device area may be measured using techniques developed previously,[35] with typical zero-volt contact areas of ~0.07−0.1 mm^2. In the presence of suprathreshold voltages, Mz (in the prechannel state with areal density P) inserts and oligomerizes to form conductive pathways (i.e., the channel state with areal density C) across the membrane. At sufficiently high voltages, Mz channels translocate to the opposite side of the membrane (i.e., the inactive state, with areal density I), which reduces their density in the bilayer and leads to depression-like behavior in the measured current. (b) Some biological synapses exhibit presynaptic STP that results from activity dependent alterations in the probability of neurotransmitter release (P_r). Low P_r synapses are considered high-pass filters as they exhibit short-term enhancement in synaptic transmission (i.e., facilitation), while medium and high P_r synapses exhibit band-pass (i.e., facilitation-then-depression) and low-pass filtering (i.e., depression), respectively.[36] (c) Representative i−v relationships obtained on a 1:1 DOPC:DPhPC membrane containing Mz exhibit nonlinear threshold switching in response to a continuous sinusoidal voltage. The pinched, hysteretic shapes indicate volatile memory resistance in MzBS. Arrows indicate the time course of voltage stimulation. (d) Current induced by a train of voltage pulses applied to a MzBS constructed from DPhPC lipids exhibits synapse like short-term paired-pulse facilitation, paired-pulse depression, and augmentation. Despite volatility, the augmentation at 70 s shows that a single voltage pulse occurring shortly after the repeated voltage pulses from 30 to 45 s elevates the conductance of the membrane to a level significantly higher than achieved during the initial pulse at 5 s.

tic calcium levels leading to an increase in neurotransmitter release after each action potential or depression (i.e., a decrease in synapse conductance) caused by depletion of synaptic vesicles available for successive action potentials. As a result, frequency-dependent dynamics in accumulation and depletion of synaptic vesicles are responsible for STP in some areas of the brain.[19,21] While the full picture of STP functionalities[16,22] and efficiency[23,24] are still being unraveled, what is known inspires the development of novel materials and devices for adaptive information processing at low energy cost.

Herein, we report a biomolecular device consisting of an insulating lipid membrane doped with monazomycin (Mz) (Figure 1a) that is capable of emulating multiple forms of STP concurrently (Figure 1b)—including facilitation-then-depression under constant stimulus frequency and augmentation[21] that persists after stimulation ends. Mz is a voltage-dependent, pore-forming antibiotic (chemical formula: $C_{72}H_{133}NO_{22}$, exact 3D conformation unknown)[25] that forms ion channels through lipid membranes (3−5 nm thick) at suprathreshold voltages.[26−29] Collectively, the formation of Mz ion channels produces nonlinear, voltage-activated memristive ion currents through the membrane (Figures 1c and S1a) that disappear in its absence (Figure S1b).

Unlike alamethicin,[30] Mz exhibits S-shaped current dynamics closer to those exhibited by potassium channels[31] and facilitation-then-depression at certain voltage amplitudes and frequencies[32]—mimicking a bidirectional form of STP (Figure 1d) responsible for sensory signal processing in the brain.[17] As in nature but unlike most previously reported artificial synapses, these forms of STP can be triggered simultaneously with a fixed input. A bidirectional response to a single fixed stimulus has been reported in few other memristive systems,[33,34] neither of which use *volatile* memory properties to process sensory information. This constitutes an important gap in realizing engineering systems with a fuller repertoire of brain-like signal processing, learning, and memory, one that is addressed by the complex short-term plasticity of MzBS. Additionally, the device is inherently biocompatible due to its phospholipid composition, allowing for potential biological interfacing as well.

Through state-based modeling, we show that Mz accumulation (channel formation) and depletion (channel inactivation) is responsible for STP exhibited in Mz-based biomolecular synapses (MzBS). To demonstrate its significance, we built an organic−inorganic hybrid model of the corneal afferent synapse that is capable of sensitization and adaptation to a real, physically transduced light signal. These devices emulate how information processing, learning, and memory occur in biological neurons, which further motivates adaptive materials for applications in biological environments such as interfacing with the brain or intrabody sensing and signal processing.

https://doi.org/10.1021/acsaelm.1c00610
ACS Appl. Electron. Mater. 2021, 3, 4448−4458

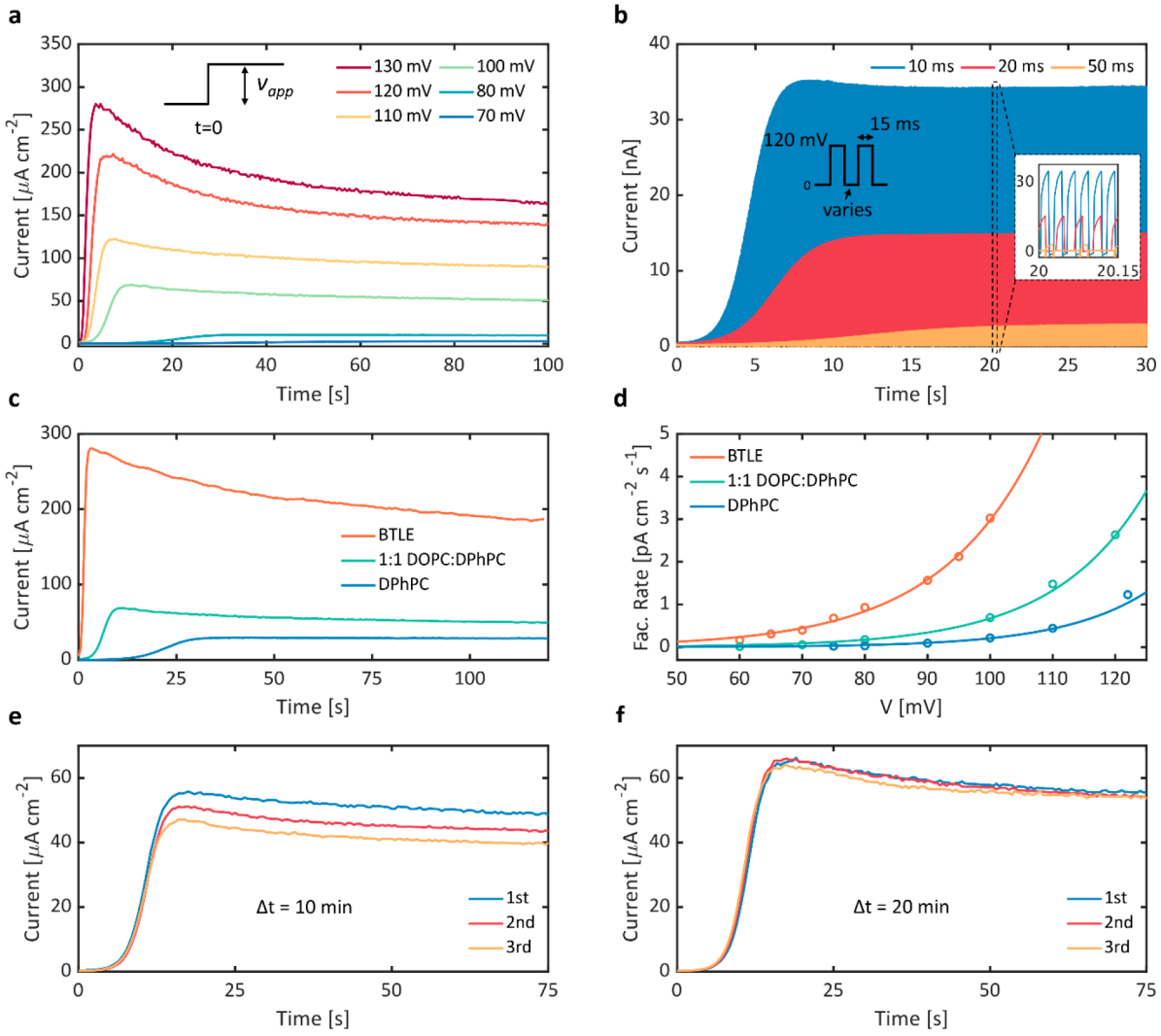

Figure 2. Dynamic responses of MzBS to applied voltages. (a, b) The equivalence of DC steps and rectangular pulses through v_{rms}. (a) Step responses for a 2.36 mM 1:1 DOPC:DPhPC membrane with 20 μg mL^{-1} of Mz. The initial rising portion of the current shifts left with increasing voltage, indicating an increased facilitation rate. The peak current also increases with voltage. The inset shows the voltage step waveform. (b) Pulsed voltage responses for a 2.36 mM 1:1 DOPC:DPhPC membrane with 20 μg mL^{-1} of Mz for three OFF times. The top inset describes the shape and time course of the voltage waveform, which varies by "off" time. A low OFF time corresponds to a higher frequency and a larger value of v_{rms}. v_{rms} values are ~92.6 mV for 10 ms OFF, ~78.3 mV for 20 ms OFF, and ~57.5 mV for 50 ms OFF. The lower inset shows a brief section of the graph to show the spike shapes. (c, d) The effects of composition on MzBS properties. (c) Step responses for three membrane compositions at 100 mV. BTLE shows the fastest facilitation and highest peak current, as well as largest percent inactivation; see Table 1 for values. (d) Exponential relationship between the current facilitation rate and the transmembrane potential. Rates were determined by fitting a single-term exponential to the first inflection point of the S-shaped current using MATLAB (Figure S5). (e, f) Augmentation and recovery in a 1:1 DOPC:DPhPC device with 20 μg mL^{-1} of Mz after repeated 100 mV steps. In (e), the MzBS is stimulated with three 90 s duration and 100 mV steps with 10 min of rest at 0 mV between stimulations. In (f), the rest time is increased to 20 min.

2. RESULTS AND DISCUSSION

2.1. Device Properties. First, we probed each device with a continuous sinusoidal voltage input and recorded the induced ionic current to study the i–v characteristics of MzBS. Positive current represents flow of positive ions from the *cis* side of the bilayer to the *trans* side (ground). All two-terminal MzBS systems were assembled and characterized as described in the Exerimental Section and elsewhere.[30,37] In this work, we added Mz to both droplets such that Mz was available on both faces of the bilayer and could form ion channels at both positive and negative *cis* potentials. This choice resulted in symmetric current–voltage (i–v) relationships, such as those shown in Figure 1c and Figure S3 for an MzBS lipid bilayer formed with a 1:1 mol ratio of 1,2-dioleoyl-*sn*-glycero-3-phosphocholine (DOPC) and 1,2-diphytanoyl-*sn*-glycero-3-phosphocholine (DPhPC) lipids. These i–v relationships show frequency-dependent, pinched hysteresis, the defining characteristic of ideal memristors set forth by Chua.[38] Hysteresis is reduced at low frequencies and increases at higher frequencies, where regions of negative differential resistance (NDR) appear (Figure 1c and Figure S3a). All MzBS exhibit volatile memristance because the conductance state resets as voltage approaches 0.

Similar to alamethicin-based synapses in our prior work,[30] MzBS exhibit diode-like current responses and switching thresholds (v_{th}) in biologically relevant ranges (~25–120 mV). In contrast, MzBS shows larger i–v hysteresis at similar frequencies compared to membranes doped with alamethi-

https://doi.org/10.1021/acsaelm.1c00610
ACS Appl. Electron. Mater. 2021, 3, 4448–4458

Table 1. Mz Facilitation Rates and Depression Percentages for Membrane Types

	initial facilitation rate = ae^{bv}			$\left(\frac{C_{peak}-C_{ss}}{C_{peak}}\right)_{80mV}$ (%)
membrane type	a [pA μm^{-2} s^{-1}]	b [mV^{-1}]	R^2	
BTLE	5.56×10^{-3}	0.0627	0.998	35.52
1:1 DOPC:DPhPC	1.141×10^{-3}	0.06781	0.9995	25.15
DPhPC	1.4×10^{-4}	0.07304	0.999	11.96

cin—indicating longer retention of the facilitated conductive state—and display more pronounced NDR at the higher frequencies tested (Figure S3a). Moreover, i–v hysteresis is maintained when nominal ionic current is normalized by real-time bilayer area measurements (a unique capability of the DIB method) to remove the effect of changes in device area caused by electrowetting (denoted i above and hereafter).[30] These findings suggest that the i–v hysteresis is a direct product of voltage-driven channel kinetics and not voltage-induced membrane expansion, as was the case with alamethicin-based synapses and constitutes a critical difference between them.[39]

Further, we discovered that MzBS stimulated by trains of voltage pulses exhibited complex dynamic responses not possible in most memristors. For instance, consider a DPhPC MzBS device stimulated by a series of brief pulses in between two reading pulses (Figure 1d). The first reading pulse (500 ms, 150 mV) shows a peak current <20 nA. Then it is stimulated with a high-frequency pulse series (50 ms on, 50 ms off, 150 mV) that produces increasing current peak amplitudes (paired-pulse facilitation), to more than 110 nA within the first 5 s of the stimulus, that then decays to ∼100 nA as the pulses continue (paired-pulse depression). This bidirectional behavior in response to a fixed voltage amplitude and frequency has not been shown before in a biomolecular device and is rare in other memristors.[10−14] In addition, the peak current of ∼40 nA induced by the final reading pulse shows the MzBS retains higher conductance than observed with the first reading pulse. This feature indicates a remembered enhancement of synapse conductivity that outlasts the excitation. This form of activity-dependent adaptation in biological synapses is called augmentation (Figure 1b), which occurs in MzBS due to slow ejection of residual Mz from the bilayer when voltage is below v_{th}, eventually resulting in a complete reset back to prestimulus conductivity.[19]

We studied three different types of MzBS devices to explore the impact of lipid type on device properties. While MzBS assembled from either synthetic DPhPC lipids only or naturally derived porcine brain total lipid extract (BTLE) showed qualitatively similar i–v relationships and hysteresis trends with respect to frequency (Figure S3), the choice of membrane lipids strongly affects the switching threshold and hysteresis shape given the same input. A DPhPC membrane formed between droplets with 20 μg mL^{-1} Mz exhibits a higher switching threshold (∼110 mV) compared to one constructed from porcine brain total lipid extract (BTLE) with only 1 μg mL^{-1} Mz in each droplet (∼55 mV) (Figure S3b,c). Mz insertion properties are documented to be highly concentration and lipid dependent.[28,29,32,40,41] Mz in BTLE showed permanent insertion and produced currents that were beyond the measurement capabilities of our devices at 20 μg mL^{-1}, so 1 μg mL^{-1} was chosen to produce synapses with similar current densities and insertion thresholds to the other devices.

The memristive and bidirectional changes in conductance motivated us to understand the reasons for these dynamics and the contributions of Mz channels. To do so, we measured the induced current density (i) to DC voltage steps on MzBS assembled with different lipid types. The responses plotted in Figure 2 and S4 are consistent with those obtained in prior work.[31] At applied potentials (v) above v_{th}, Mz-doped membranes exhibit an increase in ionic current whose rates and shapes depend on the DC voltage, the RMS voltage for an applied pulse train, and lipid composition (Figure 2a, 2b, and 2c, respectively). Figure 2a shows how the shape and amplitude of current density through a DOPC:DPhPC membrane changes for steps increasing from 70 to 130 mV. These traces show that fast, bidirectional plasticity (similar in rate and magnitude to that observed in BTLE bilayers at 100 mV) occurs at voltages above ∼100 mV, while slow, saturating responses occur at voltages between 60 and 80 mV. Similarly, a DPhPC bilayer (which exhibited the slowest response in Figure 2c) can exhibit fast, facilitating-then-depressing responses at similar speeds and peak current densities as obtained with BTLE (Figure S4), but only at voltages higher than 120 mV.

Figure 2b displays responses of the same membrane type to 120 mV, 15 ms square pulses with various OFF times (10, 20, and 50 ms). All types of MzBS devices exhibit facilitation-then-depression when pulses are separated by short OFF times (10 ms, Figure S6). Longer OFF times (20 and 50 ms) only exhibit facilitation, where peak current grew with successive pulses until reaching a steady state (Figure 2b, Figure S6). Further, the rate of facilitation for each device (Table 1, Figure S6) is proportional to the frequency of the pulse wave, where higher frequency (i.e., higher voltage RMS value) produces higher rates of facilitation. Like their biological counterparts, higher rates of facilitation can be followed by depression under continued stimulus for certain synapses. Whereas this arises from the depletion of vesicles in biological synapses,[19] it stems from inactivation of Mz in MzBS.[32]

Figure 2c shows that membrane composition strongly influences the voltage-induced current response. For example, the current through a DPhPC bilayer rises slowly in an S-shaped fashion to a stable density of 28 μA cm^{-2}, whereas induced currents at the same voltage (100 mV) through DOPC:DPhPC and BTLE membranes exhibit progressively faster and larger current responses that peak and decay. The latter show bidirectional (facilitation-then-depression) time courses similar to the response in Figures 1b and 2d generated by pulsed inputs, indicating that v_{rms} and not $|v|$ governs the dynamic response. BTLE represents the most biologically relevant composition herein. Devices assembled with it—and with only 1–2 μg mL^{-1} of Mz in the droplets—consistently show higher peak current densities, faster rates of channel formation, and larger percentage drops during depression (Figure 2c,d). In contrast, MzBS formed from DOPC:DPhPC or DPhPC membranes (with 20 μg mL^{-1} Mz in the droplets) exhibited slower, smaller increases in current at comparable voltages. Table 1 compares facilitation rates, which were found to rise exponentially with voltage (Figure 2d), and depression

https://doi.org/10.1021/acsaelm.1c00610
ACS Appl. Electron. Mater. 2021, 3, 4448−4458

amounts for the three lipid compositions. See Supplementary Discussion for effects of lipid composition and membrane fluidity on Mz.

In addition to complex and bidirectional forms of STP, MzBS devices retain memories longer than alamethicin-based synaptic membranes, which reset in less than a second.[30] Specifically, we observed the MzBS maintain an increased conductivity compared to a prefacilitated state for up to ∼2−3 min after voltage is removed, as well as decreased peak conductance for ∼10−15 min between subsequent stimulation. The results in Figure 2e and 2f demonstrate the latter. Currents are measured for successive applications of 100 mV steps, with intermittent rest periods at 0 mV for either 10 (Figure 2e) or 20 min (Figure 2f). Maximum ionic current in a 1:1 DOPC:DPhPC MzBS decreases with sequential steps when allowed a 10 min rest (Figure 2e), but initial conductance restores with a 20 min rest (Figure 2f). The recovery rate between applied voltages can also be tuned with composition (Figure S4d), suggesting that memory duration is influenced by the kinetics of Mz as discussed above. These examples of memory duration can be explained by two mechanisms, respectively: 1) Mz monomers remain in the membrane (∼2−3 min) before exiting when voltage drops below v_{th}, allowing continual but diminishing chances to reoligomerize and 2) Mz inactivation depletes (∼10−15 min) the store of available channel-forming species on the *cis* side after a depressing stimulation.

2.2. Modeling and Simulations. Past efforts to mathematically model the voltage-dependent conductance increases caused by Mz established a theoretical basis for insertion and channel formation.[28,29,32,40−43] However, far fewer models[43] have included the dynamics of facilitation-*then*-depression (often referred to simply as "inactivation") of interest herein. As such, we chose to leverage an empirical, kinetics-based approach solely for describing the dynamic, synapse-like electrical behaviors of our devices. Instead of describing the mechanisms of single channel transitions, this approach uses measurements of ionic current and device contact area to compactly model the aggregate channel density in the membrane. Development of compact device models is particularly common for understanding complex behaviors in neuromorphic devices.[44]

Prior research establishes that voltage initiates Mz channel formation via insertion and oligomerization[40,42,43] and inactivation occurs via either Mz translocation to the opposite side of the bilayer[32] or disaggregation of conductive oligomers.[43] We choose three states to describe the distribution of Mz species in a bilayer. We categorize them as nonconductive prechannels (P), conductive channels (C), and inactived channels (I) (Figure 1a). Using this notation, the current density, i, in a MzBS is described by eq 1:

$$i(t) = G_u C(v, t)\, v(t) \tag{1}$$

where G_u is the average unit conductance (∼5 pS)[28] of one Mz channel and C represents the number of Mz channels per unit area of the MzBS as a function of voltage, v, and time, t. The product of G_u and C represents the reciprocal of memristance. To better understand the dynamic step responses and i−v characteristics of MzBS, we developed a three-state model described by the following molecular kinetic style schemes:

$$P \underset{k_{1r}}{\overset{k_{1a}}{\rightleftarrows}} C \tag{2}$$

$$P + C \xrightarrow{k_{1b}} 2C \tag{3}$$

$$C \underset{k_{2r}}{\overset{k_2}{\rightleftarrows}} I \tag{4}$$

and

$$N_b(v) = P + C + I \tag{5}$$

where the P, C, and I represent the areal densities in the three Mz states; parameters k_{1a}, k_{1b}, k_{1r}, k_2, and k_{2r} represent reaction rate constants that govern transitions between states; and N_b represents the total number of active Mz species in the system. As shown, Mz in the prechannel state may transition to the channel state and Mz in the channel state may either return to the prechannel state or be driven to the inactive state. We consider both reactions to be reversible and that Mz prechannels may form channels via either a noncatalytic (eq 2) or an autocatalytic (eq 3) pathway.[40] These reactions are described by first-order differential equations:

$$\frac{dP}{dt} = -k_{1a}P - k_{1b}CP + k_{1r}C \tag{6}$$

$$\frac{dC}{dt} = k_{1a}P + k_{1b}CP - k_{1r}C - k_2C + k_{2r}I \tag{7}$$

and

$$\frac{dI}{dt} = k_2C - k_{2r}I \tag{8}$$

Equations 6 and 7 introduce nonlinearities due to the products of C and P. While the nominal values or reaction rate parameters are unknown *a priori*, we expect them to be functions of voltage of the form[40,41]

$$k_n(v) = k_n^0 e^{aqev/k_BT} \tag{9}$$

where k_n^0 is the parameter value at 0 V, a is a factor dependent on device composition (see supplementary discussion in the Supporting Information), q is the average molecularity of the Mz channel, e is the elementary electric charge, v is the applied voltage, k_B is the Boltzmann constant, and T is temperature. Assuming the charge on Mz is +1, q is 5, and the temperature is 298 K, this reduces eq 9 to

$$k_n(v) = k_n^0 e^{0.1946av} \tag{10}$$

To estimate k_n^0 and a values for each rate constant and understand how voltage and device composition affect channel kinetics, we extracted values of some parameters by employing theoretical analysis of the kinetic model at three limiting cases and then performed a series of constrained nonlinear minimizations to fit numerical solutions of eqs 6−8 to measured current responses induced by fixed voltage steps (Figures 2 and S4) to determine the remaining unobservable rate constants. First, in the limiting case where I is 0 and C is small (i.e., at the onset of applied voltage), we can reduce the linear terms in eq 7 containing C and I to 0. We do not reduce the nonlinear term containing C to 0 because k_{1b} should be much larger than k_{1a}.[29] Therefore, any amount of C will cause the autocatalytic term to dominate. We use this justification further to set the k_{1a} term to 0, resulting in

$$\frac{dC}{dt} = k_{1b}CP \tag{11}$$

https://doi.org/10.1021/acsaelm.1c00610
ACS Appl. Electron. Mater. 2021, 3, 4448−4458

Table 2. Parameter Voltage Trends and Values Used to Produce the Simulations in Figure 3g–i and Figure S5c,d in the Supporting Information

parameter voltage trends	parameter values [units]	BTLE	1:1 DOPC:DPhPC	DPhPC
$k_{1b} = k_{1b}^0 e^{0.1945Sav}$	k_{1b}^0 [pA μm^{-2} s^{-1}]	0.058	1.1×10^{-3}	1.4×10^{-4}
	a [mV^{-1}]	0.325	0.349	0.375
$N_b = N_b^0 e^{0.1945Sav}$	N_b^0 [channels μm^{-2}]	4.8×10^{-3}	1.0×10^{-4}	1.9×10^{-5}
	a [mV^{-1}]	0.374	0.479	0.529
$k_2 = k_2^0 e^{0.1945Sav}$	k_2^0 [channels μm^{-2} s^{-1}]	2.1×10^{-6}	1.5×10^{-6}	5.1×10^{-12}
	a [mV^{-1}]	0.514	0.422	0.862
$k_{2r} = k_{2r}^0 e^{0.1945Sav}$	k_{2r}^0 [channels $\mu m^{-2} s^{-1}$]	3.4×10^{-5}	1.1×10^{-4}	1.9×10^{-7}
	a [mV^{-1}]	0.406	0.249	0.469
k_{1a}	[channels μm^{-2} s^{-1}]	3.7×10^{-3}	4.4×10^{-4}	8.9×10^{-4}
k_{1r}	[channels μm^{-2} s^{-1}]	0.0438	0.242	0.314

Because P is very large compared to C at times close to 0, we treat the product $k_{1b}P$ as a constant and solve eq 11 for C, yielding

$$C(t) = c_0 e^{k_{1b}t} \tag{12}$$

Equation 12 is equivalent to the exponential model fitted to the initial current facilitation rates as seen in Figure 2d and Table 1. Therefore, this first constraint reveals that k_{1b} is equal to the rate constant for facilitation determined from the initial rate of increase in i. Converting the parameters in Table 1 to a form consistent with eq 10 results in the k_{1b} values provided in Table 2. Examples of facilitation rate fitting to the first inflection point of current can be seen in Figure S5a.

Next, we consider the onset of depression, where C achieves its peak value (C_{peak}). When $C = C_{peak}$, we assume that $I \approx 0$ and $dC/dt = -dI/dt$. This leads to

$$\frac{dC}{dt} = -k_2 C \tag{13}$$

Solving for C results in

$$C(t) = c_0 e^{-k_2 t} \tag{14}$$

For small values of time past the peak, this can be approximated as a line with the equation:

$$C(t) = -k_2 t + C_{peak} \tag{15}$$

We can therefore estimate k_2 by calculating the slope of C *vs* t immediately following the onset of depression after achieving C_{peak}. To standardize the fitted region, we use the first n points of the inactivating current that corresponds to a 10% drop in C. Example fits are shown in Figure S5b in the Supporting Information.

The final constraint we impose allows us to estimate k_{2r}. We know that at steady state, $dI/dt = 0$, which allows the construction of the steady state relation between k_2 and k_{2r} of the form

$$\frac{k_2}{k_{2r}} = \frac{I_{ss}}{C_{ss}} \tag{16}$$

where the subscript ss denotes the steady state values. Following the same assumptions that led to eq 13, we know that I_{ss} can be accounted for by the difference between C_{peak} and C_{ss} because I started at ~0. Substituting this into eq 16 and rearranging yields

$$k_{2r} = k_2 \frac{C_{ss}}{C_{peak} - C_{ss}} \tag{17}$$

To summarize, we can estimate k_{1b}, k_2, and k_{2r} directly from the current traces obtained during increasing step voltages, leaving N_b, k_{1r}, and k_{1a} to be fit by nonlinear minimization between the full model and the measured current density (details in Experimental Section). The results of our estimations and their exponential voltage trends may be found in Figure 3a–f. Also contained in Figure 3g–i are generalized simulations of step responses for each MzBS compositions whose respective parameters are generated from the voltage-dependent expressions or using an averaged value when no strong voltage dependence was determined. Exact values for fit equations and static values used for these simulations may be found in Table 2.

We find that all directly estimated parameters (k_{1b}, k_2, and k_{2r}) have strong exponential trends, while only N_b showed a strong trend from the remaining fitted parameters. As indicated by the error bars (±1 standard deviation) in Figure 3a,b,d, the fitting produced consistent values for the reaction rate constants across all voltages. The voltage-generalized parameters predict the behavior of the steps in Figure 3g–i, where the colored circles are the experimental data, and the black lines are the outputs of model simulations. The divergence of simulations at higher voltages in Figure 3i for a BTLE device are likely affected by our estimation of C_{ss} using the average current obtained during the final 1s of the step; clearly, the BTLE devices have not reached steady state yet. We also find that the parameters listed in Table 2 can be used to simulate device current induced by a dynamic sinusoidal input, as seen in Figure S5d.

2.3. Organic–Inorganic Hybrid Afferent Synapse.

Biological systems dynamically adapt their sensory networks to effectively relay fluctuating sensory signals through adaptation and sensitization.[16] Both frequency-filtering functions—exclusively conveyed through STP—allow visual systems (Figure 4a) to increase dynamic range in response to changes in contrast.[45−47] Additionally, synapses in the brain adjust their weights through multiple mechanisms that span multiple time scales to affect signal transmission.[15,19−21,46,48] MzBS show dynamics on multiple time scales that are produced by a single input and are affected by device stimulation history (Figure 2), as in biology. These properties of MzBS suggest that it may be used as an adaptive element for signal processing of sensory input to bring brain-like, biologically relevant functionality to existing solid-state systems.[16] We investigated this implementation by assembling an organic–inorganic hybrid afferent synapse consisting of a photosensor-neuron system of 2 solid-state, leaky-integrate-

https://doi.org/10.1021/acsaelm.1c00610
ACS Appl. Electron. Mater. 2021, 3, 4448−4458

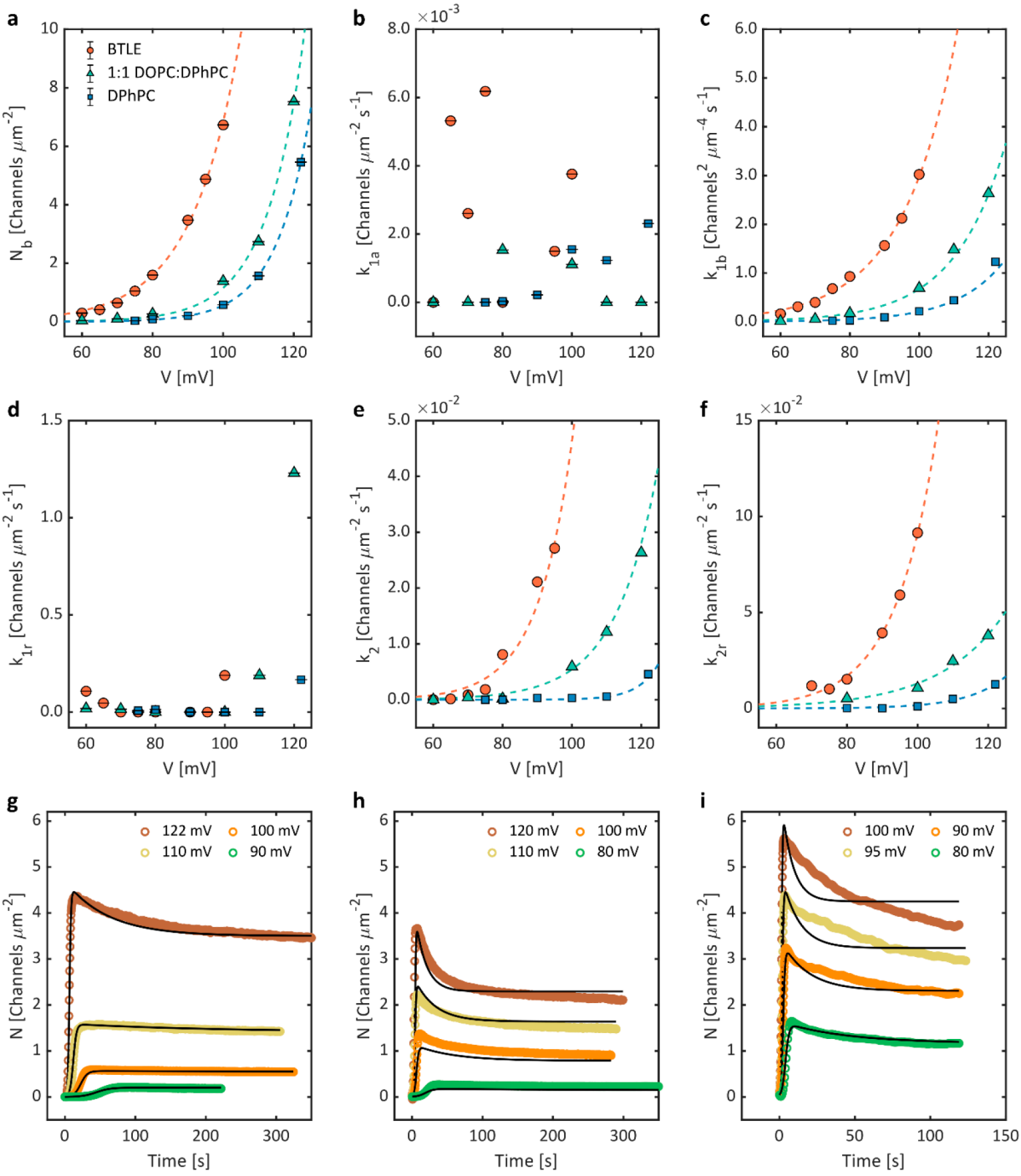

Figure 3. Parameter fitting and step simulations across voltage and composition. Error bars for fitted parameters are ±1 standard deviation from 20 simulations with randomized seed values for fitted parameters. Dashed lines correspond to an exponential fit in the form of eq 10. (a) Fitted N_b values. (b) Fitted k_{1a} values. (c) Estimated k_{1b} values. (d) Fitted k_{1r} values. (e) Estimated k_2 values. (f) Estimated k_{2r} values based on the trend from (e) and eq 17. (g–i) Step response ensembles using generalized parameters from panels a–f. (g) DPhPC only device, 20 μg mL^{-1} Mz. (h) 1:1 DOPC:DPhPC device, 20 μg mL^{-1} Mz. (i) BTLE device, 1 μg mL^{-1} Mz.

and-fire neurons previously developed by Weiss et al.[49] connected via a BTLE MzBS (Figure 4b and Figure S7).

Neuron 1 receives current from a biased photoresistor (PR), whose resistance is modulated by light from five white LEDs. At a fixed supply voltage, the intensity of light controls the electrical current to neuron 1, dictating its spiking frequency. The MzBS connects neuron 1 to neuron 2, such that their potential difference controls the flow of ionic current through the MzBS to induce firing of neuron 2. Figure 4c shows that the firing frequency of neuron 1 depends on the level of light and does not vary in time. *High*, *medium*, and *low* levels correspond to 5, 3, and 1 LED(s) acting on the PR, which causes firing rates of 60, 57.5, and 55 Hz in neuron 1 with equivalent v_{rms} of 110, 107.4, and 105 mV, respectively. Figure 4d (left axis, open circles) shows the corresponding dynamic currents through the Mz caused by these outputs from neuron 1. The overlaid triangles (right axis) show the dynamic frequency at which neuron 2 fires in response. The

https://doi.org/10.1021/acsaelm.1c00610
ACS Appl. Electron. Mater. 2021, 3, 4448–4458

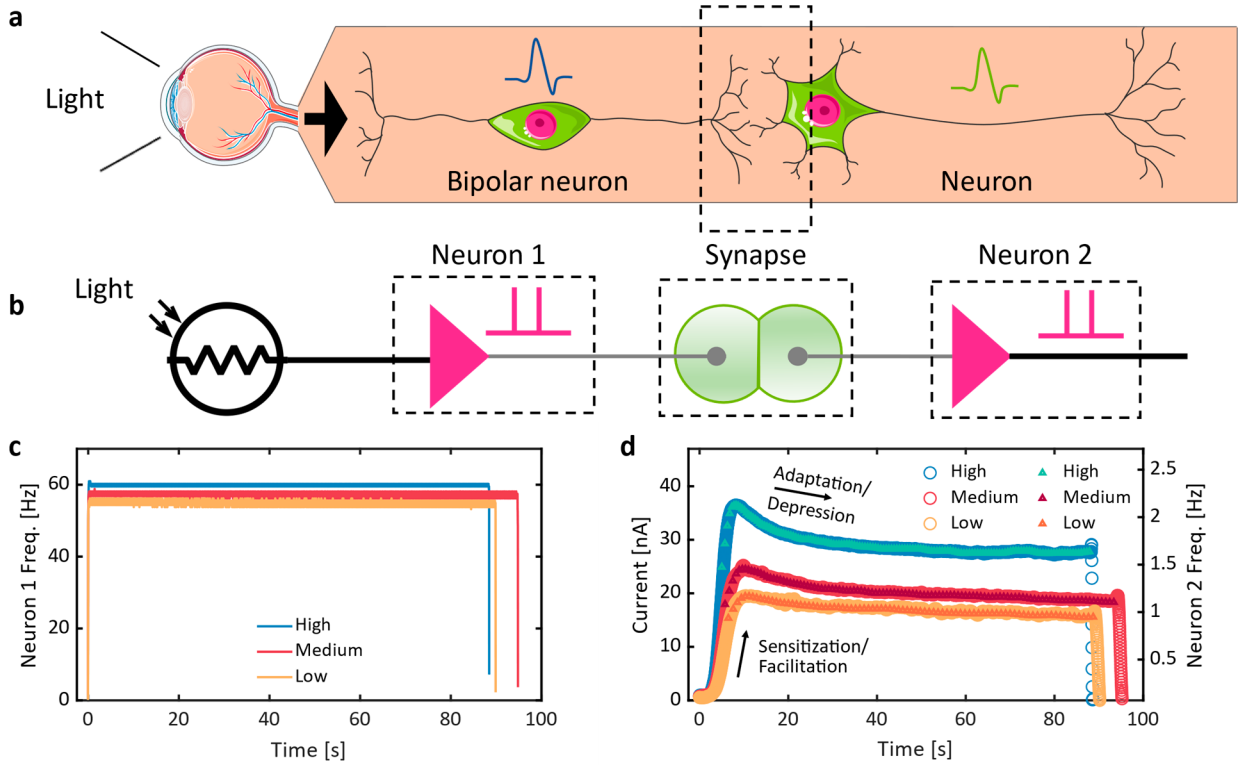

Figure 4. Synaptic capabilities of MzBS between solid-state neurons. (a) A schematic of an afferent neuron and synapse connected to the eye. (b) Hybrid afferent synapse, with a Mz-doped lipid bilayer acting as the connection between two solid state neurons. Full circuit diagram can be found in Figure S7. (c, d): LEDs are switched on at time = 0 s. (c) Frequency of neuron 1 firing rate in response to *high*, *medium*, and *low* light levels. Neuron 1 begins firing immediately and maintains a constant firing rate while the LEDs are on. (d) Left axis, open circles: Peak synapse currents of a BTLE MzBS containing 1 μg/mL Mz at *high*, *medium*, and *low* light intensity responding the output voltage from neuron 1. Right axis, triangles: the resulting firing frequency of neuron 2, determined from the interval between voltage pulses output by neuron 2, which had fixed widths of 15 ms as set by the neuron circuitry (Figure S7).

proportionality between the bidirectional ion current and the firing frequencies of neuron-2 demonstrates that MzBS plasticity adaptively filters the responses of neuron 1. The reduced firing rate of neuron 2 (1−2.5 Hz) compared to neuron 1 (55−60 Hz) is caused by the high resistance of the MzBS (~MΩ), which limits the rate of neuron 2 charging and firing.

If it is necessary, some ways to increase the firing rate of neuron 2 are increasing synapse conductivity by increasing bilayer area, increasing Mz concentration, changing lipid composition, or modifying the circuitry to lower the accumulation threshold of neuron 2. The important feature is that the MzBS converts the frequency information from neuron 1 into an adaptive current that controls the activity of neuron 2. In contrast, in the absence of dynamic and history-dependent ion channels in the synapse, the resistance of the lipid membrane would be too high (>10 GΩ) to allow for enough current to charge neuron 2.

This demonstration shows that our biomolecular soft matter device can directly interface with existing solid state neuromorphic hardware. Its processing capabilities require no software or additional complicated circuit elements and operate at very low voltages, thereby decreasing power dissipation. We also show that it can respond directly to a sensory stimulus, making it a feasible inclusion in robotic systems requiring sensory processing and artificial intelligence algorithms using time-varying inputs.

3. CONCLUSION

A two-terminal device that exhibits concurrent forms of STP is a boon for brain-like computing. Many devices have demonstrated one or more forms of STP independently, but only upon shifting the operating range or stimulus. The MzBS reported here show multiple forms of STP without significantly changing the mode or range of operation. *Facilitation*, *depression*, and *augmentation* are key characteristics of neural synapses and networks that must be understood well to make advancements at the same pace as disciplines under the umbrella of artificial intelligence. An MzBS, with its voltage-dependent inactivation mechanism, opens possibilities in the design space for other biomimetic systems and encourages the review of what neuroscientists have already uncovered, so that we may take inspiration from a phenomenon such as synaptic vesicle depletion, for instance. Moreover, a biomolecular approach is inherently biocompatible and low power; the former being important in the field of biomedical engineering, and the latter being useful in almost every application.

We envision networks of MzBS with tunable characteristics that can be used as a first line of autonomic signal processing in visual, haptic, or even olfactory sensors; systems which require desensitization and slow "forgetting" to be effective in their purpose of assessing novelty and importance of incoming signals. The brain has evolved to be maximally efficient, and these properties of sensory processing are key factors to realize something similar in modern AI/robotics. We are certain

https://doi.org/10.1021/acsaelm.1c00610
ACS Appl. Electron. Mater. 2021, 3, 4448−4458

continuing in this direction will yield new and interesting results.

4. EXPERIMENTAL SECTION

4.1. Vesicle and Solution Preparation. Lipids were purchased from Avanti Polar Lipids (Alabaster, AL). Dry lipid films were produced by fully evaporating chloroform dissolved stock under nitrogen stream and then additionally desiccated for an hour under vacuum. Dry films were rehydrated in ultrapure water at a concentration of 5 mg mL^{-1} to make stock aqueous lipid solutions. Lipid mixtures were made by mixing chloroform solutions of each prior to desiccation. Stock solutions were frozen and thawed four times and mixed well before being passed 11 times through a 100 nm extrusion filter (Whatman). Lipid stocks were combined with NaCl and 3-(*N*-morpholino)propanesulfonic acid (MOPS) from Sigma (St. Louis, MO) and monazomycin from Cayman Chemical (Ann Arbor, MI) to obtain final concentrations of 2 mg mL^{-1} lipids, 100 mM NaCl, 10 mM MOPS, and 1−20 μg mL^{-1} Mz, depending on lipid type (1−2 for BTLE, 20 for others). Mz solution pH was consistently measured to be near 6 and was not modified for device testing.

4.2. Membrane Electrical and Optical Measurements. Most current measurements were performed using an Axopatch 200B patch clamp amplifier and Digidata 1440A or 1550B data acquisition system (Molecular Devices, San Jose, CA) at a sampling frequency of 5 kHz. A Faraday cage was used to lessen noise from the environment, resulting in <1 pA RMS noise. Voltages were output by the Axopatch or an NI DAQ (National Instruments, Austin, TX) running custom LabView script. The membrane area was assessed by analysis of images obtained in brightfield using a QICAM (Q Imagining) or xiC (Ximea) camera attached to an inverted microscope as outlined previously.[35] Measurements of synapse current in the hybrid neuron setup were made using a Keithley DMM6500 with a sampling rate of 60 Hz. Neuron voltages were measured by the Digidata 1440A at 5 kHz. All testing was performed at ambient room temperature (~23 C). Droplet volumes of 250−300 nL were used for all tests, resulting in typical membrane areas between 0.07 and 0.1 mm^2.

4.3. Fitting and Simulations. To describe the current−voltage (i−v) response of Mz-doped membranes, a memristive model and kinetic molecular approach are combined. The dynamic density of channels is defined using a kinetic model based on a simplified "insertion-aggregation" process theorized for channels that bind to the membrane surface and oligomerize once inside the membrane[40,43] and is represented by eqs 1−4. Parameters k_{1b}, k_2, and k_{2r} were estimated in accordance with eqs 12, 15, and 17 for each voltage level and device. Current density up to the first inflection point calculated numerically after LOESS smoothing using a 2 s window was used to calculate k_{1b}, examples of which can be seen in Figure S5a, as well as linear fitting of eq 15 to the onset of depression in Figure S5b. Model fitting was done iteratively by simulating the dynamic responses of eq 6−8 with ode45 (MATLAB) and minimizing the root-mean-square error (RMSE) between the simulated channel densities, C, and measured channel densities computed from raw current density ($C_{meas} = i/(G_u v)$) using the nonlinear minimization function *fminsearch* in MATLAB (Mathworks, Natick, MA). Initial guesses for reaction rate constants not predetermined by eqs 12, 15, or 17 were randomized between 0 and 1 at the start of each fit routine to reduce the dependence of fitted parameters on initial guesses for their values. Parameters that were pre-estimated were not changed. The initial guess for N_b was estimated from the peak channel density of each response, typically twice the C_{peak} achieved.

To capture the voltage-dependent step behaviors of the MzBS in Figure 3g−i, the voltage depenent reaction parameters and N_b need to be generalized by finding their exponential voltage trends. Given three freely changing parameters and only 1 measurable state, we anticipated the possibility of nonunique solutions of parameters yielding comparable fits. Therefore, nonlinear minimizations were performed many times on each set of step responses for a given device composition as presented in Figure 3. Parameter solutions from the first 20 iterations that yielded simulated results with a final normalized value RMSE (divided by current density range) < 5% were accepted for assessing voltage trends. Each marker represents fit results of an individual step response (indicated by voltage) from the same device.

■ ASSOCIATED CONTENT

Supporting Information

The Supporting Information is available free of charge at https://pubs.acs.org/doi/10.1021/acsaelm.1c00610.

Figures of device memristive properties, device repeatability and endurance, membristive i-v hysteresis, voltage step inputs, parameter estimateion and additional simulations, pulsed voltage responses, organic−inorganic circuit representation; tables of repeatability metrics, inorganic−organic hybrid circuit component values; and discussion to provide more detail about device properties, parameter estimation, and circuit specifics (PDF)

■ AUTHOR INFORMATION

Corresponding Authors

Joseph S. Najem − *Department of Mechanical Engineering, The Pennsylvania State University, University Park, Pennsylvania 16082, United States*; Email: jsn5211@psu.edu

Stephen A. Sarles − *Department of Mechanical, Aerospace and Biomedical Engineering, University of Tennessee, Knoxville, Tennessee 37916, United States*; orcid.org/0000-0002-6694-6451; Email: ssarles@utk.edu

Authors

Joshua J. Maraj − *Department of Mechanical, Aerospace and Biomedical Engineering, University of Tennessee, Knoxville, Tennessee 37916, United States*; orcid.org/0000-0001-8664-1607

Jessie D. Ringley − *Department of Mechanical, Aerospace and Biomedical Engineering, University of Tennessee, Knoxville, Tennessee 37916, United States*

Ryan J. Weiss − *Department of Electrical Engineering and Computer Science, University of Tennessee, Knoxville, Tennessee 37916, United States*

Garrett S. Rose − *Department of Electrical Engineering and Computer Science, University of Tennessee, Knoxville, Tennessee 37916, United States*

Complete contact information is available at: https://pubs.acs.org/10.1021/acsaelm.1c00610

Author Contributions

The manuscript was written through contributions of all authors. All authors have given approval to the final version of the manuscript.

Author Contributions

#J.J.M. and J.S.N. contributed equally.

Funding

This material is based on research sponsored by Air Force Office of Scientific Research grant number FA9550-19-1-0213 and Air Force Research Laboratory under agreement number FA8750-19-1-0025. The U.S. Government is authorized to reproduce and distribute reprints for Governmental purposes notwithstanding any copyright notation thereon. Financial support for J.S.N. was provided by the Department of Mechanical Engineering at The Pennsylvania State University.

Notes

The authors declare no competing financial interest.

REFERENCES

(1) Tang, J.; Yuan, F.; Shen, X.; Wang, Z.; Rao, M.; He, Y.; Sun, Y.; Li, X.; Zhang, W.; Li, Y.; Gao, B.; Qian, H.; Bi, G.; Song, S.; Yang, J. J.; Wu, H. Bridging Biological and Artificial Neural Networks with Emerging Neuromorphic Devices: Fundamentals, Progress, and Challenges. *Adv. Mater.* **2019**, *31* (49), 1902761.

(2) Xia, Q.; Yang, J. J. Memristive crossbar arrays for brain-inspired computing. *Nat. Mater.* **2019**, *18* (4), 309−323.

(3) Jeong, D. S.; Kim, K. M.; Kim, S.; Choi, B. J.; Hwang, C. S. Memristors for energy-efficient new computing paradigms. *Advanced Electronic Materials* **2016**, *2* (9), 1600090.

(4) Schuman, C. D.; Potok, T. E.; Patton, R. M.; Birdwell, J. D.; Dean, M. E.; Rose, G. S.; Plank, J. S., A survey of neuromorphic computing and neural networks in hardware. *arXiv:1705.06963* **2017**.

(5) Freeman, W. J. How and why brains create meaning from sensory information. *Int. J. Bifurcation Chaos Appl. Sci. Eng.* **2004**, *14* (02), 515−530.

(6) Kim, Y.; Chortos, A.; Xu, W.; Liu, Y.; Oh, J. Y.; Son, D.; Kang, J.; Foudeh, A. M.; Zhu, C.; Lee, Y. A bioinspired flexible organic artificial afferent nerve. *Science* **2018**, *360* (6392), 998−1003.

(7) Yoon, J. H.; Wang, Z.; Kim, K. M.; Wu, H.; Ravichandran, V.; Xia, Q.; Hwang, C. S.; Yang, J. J. An artificial nociceptor based on a diffusive memristor. *Nat. Commun.* **2018**, *9* (1), 417.

(8) Strukov, D. B.; Snider, G. S.; Stewart, D. R.; Williams, R. S. The missing memristor found. *Nature* **2008**, *453* (7191), 80−83.

(9) van de Burgt, Y.; Lubberman, E.; Fuller, E. J.; Keene, S. T.; Faria, G. C.; Agarwal, S.; Marinella, M. J.; Talin, A. A.; Salleo, A. A non-volatile organic electrochemical device as a low-voltage artificial synapse for neuromorphic computing. *Nat. Mater.* **2017**, *16* (4), 414−418.

(10) Li, Y.; Wang, Z.; Midya, R.; Xia, Q.; Yang, J. J. Review of memristor devices in neuromorphic computing: materials sciences and device challenges. *J. Phys. D: Appl. Phys.* **2018**, *51* (50), 503002.

(11) Wang, Z.; Joshi, S.; Savel'ev, S. E.; Jiang, H.; Midya, R.; Lin, P.; Hu, M.; Ge, N.; Strachan, J. P.; Li, Z. Memristors with diffusive dynamics as synaptic emulators for neuromorphic computing. *Nat. Mater.* **2017**, *16* (1), 101−108.

(12) Zhou, F.; Zhou, Z.; Chen, J.; Choy, T. H.; Wang, J.; Zhang, N.; Lin, Z.; Yu, S.; Kang, J.; Wong, H.-S. P. Optoelectronic resistive random access memory for neuromorphic vision sensors. *Nat. Nanotechnol.* **2019**, *14* (8), 776−782.

(13) Sun, L.; Zhang, Y.; Hwang, G.; Jiang, J.; Kim, D.; Eshete, Y. A.; Zhao, R.; Yang, H. Synaptic Computation Enabled by Joule Heating of Single-Layered Semiconductors for Sound Localization. *Nano Lett.* **2018**, *18* (5), 3229−3234.

(14) Kumar, M.; Singh, R.; Kang, H.; Kim, S.; Seo, H. An artificial piezotronic synapse for tactile perception. *Nano Energy* **2020**, *73*, 104756.

(15) Citri, A.; Malenka, R. C. Synaptic Plasticity: Multiple Forms, Functions, and Mechanisms. *Neuropsychopharmacology* **2008**, *33* (1), 18−41.

(16) Anwar, H.; Li, X.; Bucher, D.; Nadim, F. Functional roles of short-term synaptic plasticity with an emphasis on inhibition. *Curr. Opin. Neurobiol.* **2017**, *43*, 71−78.

(17) De Palo, G.; Facchetti, G.; Mazzolini, M.; Menini, A.; Torre, V.; Altafini, C. Common dynamical features of sensory adaptation in photoreceptors and olfactory sensory neurons. *Sci. Rep.* **2013**, *3* (1), 1251.

(18) Li, H. L.; Van Rossum, M. C. Energy efficient synaptic plasticity. *eLife* **2020**, *9*, No. e50804.

(19) Zucker, R. S.; Regehr, W. G. Short-term synaptic plasticity. *Annu. Rev. Physiol.* **2002**, *64* (1), 355−405.

(20) Dobrunz, L. E.; Stevens, C. F. Heterogeneity of Release Probability, Facilitation, and Depletion at Central Synapses. *Neuron* **1997**, *18* (6), 995−1008.

(21) Stevens, C. F.; Wesseling, J. F. Augmentation Is a Potentiation of the Exocytotic Process. *Neuron* **1999**, *22* (1), 139−146.

(22) Mochida, S. Neurotransmitter Release Site Replenishment and Presynaptic Plasticity. *Int. J. Mol. Sci.* **2021**, *22* (1), 327.

(23) Denève, S.; Alemi, A.; Bourdoukan, R. The Brain as an Efficient and Robust Adaptive Learner. *Neuron* **2017**, *94* (5), 969−977.

(24) Li, H. L.; van Rossum, M. C. W. Energy efficient synaptic plasticity. *eLife* **2020**, *9*, e50804.

(25) Nakayama, H.; Furihata, K.; Seto, H.; Ōtake, N. Structure of monazomycin, a new ionophohous antibiotic. *Tetrahedron Lett.* **1981**, *22* (51), 5217−5220.

(26) Muller, R. U.; Finkelstein, A. Voltage-Dependent Conductance Induced in Thin Lipid Membranes by Monazomycin. *J. Gen. Physiol.* **1972**, *60* (3), 263−284.

(27) Bamberg, E.; Janko, K. Single channel conductance at lipid bilayer membranes in presence of monazomycin. *Biochim. Biophys. Acta, Biomembr.* **1976**, *426* (3), 447−450.

(28) Andersen, O. S.; Muller, R. U. Monazomycin-induced single channels. I. Characterization of the elementary conductance events. *J. Gen. Physiol.* **1982**, *80* (3), 403.

(29) Muller, R. U.; Andersen, O. S. Monazomycin-induced single channels. II. Origin of the voltage dependence of the macroscopic conductance. *J. Gen. Physiol.* **1982**, *80* (3), 427.

(30) Najem, J. S.; Taylor, G. J.; Weiss, R. J.; Hasan, M. S.; Rose, G.; Schuman, C. D.; Belianinov, A.; Collier, C. P.; Sarles, S. A. Memristive Ion Channel-Doped Biomembranes as Synaptic Mimics. *ACS Nano* **2018**, *12*, 4702.

(31) Muller, R. U.; Finkelstein, A. Voltage-dependent conductance induced in thin lipid membranes by monazomycin. *J. Gen. Physiol.* **1972**, *60* (3), 263−284.

(32) Heyer, R. J.; Muller, R. U.; Finkelstein, A. Inactivation of monazomycin-induced voltage-dependent conductance in thin lipid membranes. II. Inactivation produced by monazomycin transport through the membrane. *J. Gen. Physiol.* **1976**, *67* (6), 731.

(33) Wang, Z.; Joshi, S.; Savel'ev, S. E.; Jiang, H.; Midya, R.; Lin, P.; Hu, M.; Ge, N.; Strachan, J. P.; Li, Z.; Wu, Q.; Barnell, M.; Li, G.-L.; Xin, H. L.; Williams, R. S.; Xia, Q.; Yang, J. J. Memristors with diffusive dynamics as synaptic emulators for neuromorphic computing. *Nat. Mater.* **2017**, *16* (1), 101−108.

(34) Wu, Z.; Lu, J.; Shi, T.; Zhao, X.; Zhang, X.; Yang, Y.; Wu, F.; Li, Y.; Liu, Q.; Liu, M. A Habituation Sensory Nervous System with Memristors. *Adv. Mater.* **2020**, *32* (46), 2004398.

(35) Taylor, G. J.; Venkatesan, G. A.; Collier, C. P.; Sarles, S. A. Direct in situ measurement of specific capacitance, monolayer tension, and bilayer tension in a droplet interface bilayer. *Soft Matter* **2015**, *11* (38), 7592−7605.

(36) Regehr, W. G. Short-term presynaptic plasticity. *Cold Spring Harbor Perspect. Biol.* **2012**, *4* (7), a005702.

(37) Najem, J. S.; Taylor, G. J.; Armendarez, N.; Weiss, R. J.; Hasan, M. S.; Rose, G. S.; Schuman, C. D.; Belianinov, A.; Sarles, S. A.; Collier, C. P. Assembly and characterization of biomolecular memristors consisting of ion channel-doped lipid membranes. *J. Visualized Exp.* **2019**, No. 145, e58998.

(38) Chua, L. If it's pinched it'sa memristor. *Semicond. Sci. Technol.* **2014**, *29* (10), 104001.

(39) Najem, J. S.; Taylor, G. J.; Weiss, R. J.; Hasan, M. S.; Rose, G.; Schuman, C. D.; Belianinov, A.; Collier, C. P.; Sarles, S. A. Memristive Ion Channel-Doped Biomembranes as Synaptic Mimics. *ACS Nano* **2018**, *12* (5), 4702−4711.

(40) Muller, R. U.; Peskin, C. S. The kinetics of monazomycin-induced voltage-dependent conductance. II. Theory and a demonstration of a form of memory. *J. Gen. Physiol.* **1981**, *78* (2), 201.

(41) Muller, R. U.; Orin, G.; Peskin, C. S. The kinetics of monazomycin-induced voltage-dependent conductance. I. Proof of the validity of an empirical rate equation. *J. Gen. Physiol.* **1981**, *78* (2), 171.

(42) Becucci, L.; Guidelli, R. Kinetics of Channel Formation in Bilayer Lipid Membranes (BLMs) and Tethered BLMs: Monazomycin and Melittin. *Langmuir* **2007**, *23* (10), 5601−5608.

(43) Baumann, G.; Mueller, P. A molecular model of membrane excitability. *J. Supramol. Struct.* **1974**, *2* (5−6), 538−557.

https://doi.org/10.1021/acsaelm.1c00610
ACS Appl. Electron. Mater. 2021, 3, 4448−4458

(44) Kumar, S.; Williams, R. S.; Wang, Z. Third-order nanocircuit elements for neuromorphic engineering. *Nature* **2020**, *585* (7826), 518−523.
(45) Kastner, D. B.; Baccus, S. A. Coordinated dynamic encoding in the retina using opposing forms of plasticity. *Nat. Neurosci.* **2011**, *14* (10), 1317.
(46) Nikolaev, A.; Leung, K.-M.; Odermatt, B.; Lagnado, L. Synaptic mechanisms of adaptation and sensitization in the retina. *Nat. Neurosci.* **2013**, *16* (7), 934−941.
(47) Rosa, J. M.; Ruehle, S.; Ding, H.; Lagnado, L. Crossover Inhibition Generates Sustained Visual Responses in the Inner Retina. *Neuron* **2016**, *90* (2), 308−319.
(48) Kastner, D. B.; Baccus, S. A. Coordinated dynamic encoding in the retina using opposing forms of plasticity. *Nat. Neurosci.* **2011**, *14* (10), 1317−1322.
(49) Weiss, R.; Najem, J. S.; Hasan, M. S.; Schuman, C. D.; Belianinov, A.; Collier, C. P.; Sarles, S. A.; Rose, G. S. A Soft-Matter Biomolecular Memristor Synapse for Neuromorphic Systems. *2018 IEEE Biomedical Circuits and Systems Conference (BioCAS), 17−19 Oct. 2018*; IEEE, 2018; pp 1−4.

NOTE ADDED AFTER ASAP PUBLICATION

This paper originally published ASAP on September 16, 2021. A new version was reposted on September 22, 2021 noting Dr. Joseph S. Najem as a corresponding author.

https://doi.org/10.1021/acsaelm.1c00610
ACS Appl. Electron. Mater. 2021, 3, 4448−4458